Available online at www.sciencedirect.com
ScienceDirect
Icarus 193 (2008) 359–371
ICARUS
www.elsevier.com/locate/icarus

The topography of Iapetus' leading side

Bernd Giese [a,*], Tilmann Denk [b], Gerhard Neukum [b], Thomas Roatsch [a], Paul Helfenstein [c], Peter C. Thomas [c], Elizabeth P. Turtle [d], Alfred McEwen [e], Carolyn C. Porco [f]

[a] *DLR, Institute of Planetary Research, Rutherfordstr. 2, 12489 Berlin, Germany*
[b] *Department of Earth Sciences, Freie Universität Berlin, 12249 Berlin, Germany*
[c] *Center for Radiophysics and Space Research, Cornell University, Ithaca, NY 14853, USA*
[d] *Johns Hopkins University Applied Physics Laboratory, 11100 Johns Hopkins Rd., Laurel, MD 20723, USA*
[e] *Lunar and Planetary Laboratory, University of Arizona, 1541 E. University Blvd., Tucson, AZ 85721, USA*
[f] *Cassini Imaging Central Laboratory for Operations, Space Science Institute, 4750 Walnut Street, Suite 205, Boulder, CO 80301, USA*

Received 12 December 2006; revised 15 May 2007

Available online 18 July 2007

Abstract

We have used Cassini stereo images to study the topography of Iapetus' leading side. A terrain model derived at resolutions of 4–8 km reveals that Iapetus has substantial topography with heights in the range of −10 km to +13 km, much more than observed on the other middle-sized satellites of Saturn so far. Most of the topography is older than 4 Ga [Neukum, G., Wagner, R., Denk, T., Porco, C.C., 2005. Lunar Planet. Sci. XXXVI. Abstract 2034] which implies that Iapetus must have had a thick lithosphere early in its history to support this topography. Models of lithospheric deflection by topographic loads provide an estimate of the required elastic thickness in the range of 50–100 km. Iapetus' prominent equatorial ridge [Porco, C.C., and 34 colleagues, 2005. Science 307, 1237–1242] reaches widths of 70 km and heights of up to 13 km from their base within the modeled area. The morphology of the ridge suggests an endogenous origin rather than a formation by collisional accretion of a ring remnant [Ip, W.-H., 2006. Geophys. Res. Lett. 33, doi:10.1029/2005GL025386. L16203]. The transition from simple to complex central peak craters on Iapetus occurs at diameters of 11 ± 3 km. The central peaks have pronounced conical shapes with flanking slopes of typically 11° and heights that can rise above the surrounding plains. Crater depths seem to be systematically lower on Iapetus than on similarly sized Rhea, which if true, may be related to more pronounced crater-wall slumping (which widens the craters) on Iapetus than on Rhea. There are seven large impact basins with complex morphologies including central peak massifs and terraced walls, the largest one reaches 800 km in diameter and has rim topography of up to 10 km. Generally, no rings are observed with the basins consistent with a thick lithosphere but still thin enough to allow for viscous relaxation of the basin floors, which is inferred from crater depth-to-diameter measurements. In particular, a 400-km basin shows up-domed floor topography which is suggestive of viscous relaxation. A model of complex crater formation with a viscoplastic (Bingham) rheology [Melosh, H.J., 1989. Impact Cratering. Oxford Univ. Press, New York] of the impact-shocked icy material provides an estimate of the effective cohesion/viscosity at 0.04 ± 0.01 MPa/0.6 ± 0.2 GPa s. The local distribution of bright and dark material on the surface of Iapetus is largely controlled by topography and consistent with the dark material being a sublimation lag deposit originating from a bright icy substrate mixed with the dark components, but frost deposits are possible as well.

Keywords: Iapetus; Saturn, satellites; Satellites, shapes; Satellites, surfaces; Cratering

1. Introduction

Little has been known about the topography of Iapetus, but topography is important in understanding the geology of the surface and the thermal evolution of the lithosphere. The Voyager spacecraft imaged Iapetus only from distant positions (8.5 km/pxl at best) and with poor radiometric resolutions (Smith et al., 1981, 1982), which has hitherto prevented detailed topographic studies. Limited topographic information could be inferred from stereo image pairs compiled to anaglyph images (Croft, 1991) wherein individual scarps were identified and the morphology of craters was discerned, but no quantitative topo-

* Corresponding author. Fax: +49 30 67055402.
E-mail address: bernd.giese@dlr.de (B. Giese).

0019-1035/$ – see front matter
doi:10.1016/j.icarus.2007.06.005

graphic data were derived. Moreover, the analysis was restricted to the bright North Pole and anti-Saturn facing hemisphere of Iapetus and no information was attained for its dark leading side. Denk et al. (2000) carried out limb measurements in Voyager images and detected a huge bulge and mountain-like structures with heights of up to 25 km. These were first indications of relatively large topography on Iapetus.

Cassini imaging has substantially improved the situation. During Cassini's encounter with Iapetus on 31 Dec. 2004, the Imaging Science Subsystem (ISS) on board has taken images of Iapetus with resolutions down to 0.8 km/pxl (Porco et al., 2005). These images (covering Iapetus' dark leading side) are of excellent radiometric resolution and allowed us to carry out the first detailed topographic mapping of this satellite.

Our mapping approach is based on methods of photogrammetry that include digital image correlations and the generation of a Digital Terrain Model (DTM). It is focused on the high-resolution topography of the surface. In a different approach, global shape modeling has been carried out to determine the figure of Iapetus (Thomas et al., 2008). Here, we make use of the ellipsoidal shape parameters determined by shape modeling and show the topography of Iapetus relative to this surface. The DTM we derived has horizontal resolutions of 4–8 km, suitable for studying the morphology of the surface over scales larger than 10 km, including Iapetus' prominent equatorial ridge (Porco et al., 2005). Moreover, using images taken in Saturnshine, a separate smaller DTM could be derived covering part of Iapetus' trailing side. This DTM bears additional information on crater morphologies and on the equatorial ridge.

In this paper, we present the topography of Iapetus based on Cassini imaging and show implications for crater formation, the formation of the equatorial ridge, the nature of bright and dark terrains, and for lithospheric thickness from topography.

2. Methods and data base

For the topographic modeling of Iapetus we applied methods of digital photogrammetry described in detail in previous papers (Giese et al., 1998, 2006a). Here, we give just a short outline of the procedure.

In the first step, a control-point network was set up to correct the camera pointing angles (s/c positions were fixed throughout the modeling) within a least-squares adjustment. Next, conjugate points were determined in stereo image pairs by methods of automated digital image correlation. Third, ground surface points (x, y, z) were computed from the conjugate points and referenced to a topographic datum to obtain the points' latitudes, longitudes and elevations. Fourth, latitudes and longitudes were subjected to a map projection and then interpolated to form a contiguous DTM grid. Grid points that could not be interpolated (in lack of points in the surroundings) were left as gaps. Finally, individual DTMs derived from the stereo image pairs were mosaicked to a single DTM.

Nominal spacecraft orbit and camera pointing data and the camera calibration parameters required in the calculations were gathered from NAIF-SPICE kernels delivered by the Cassini flight project.

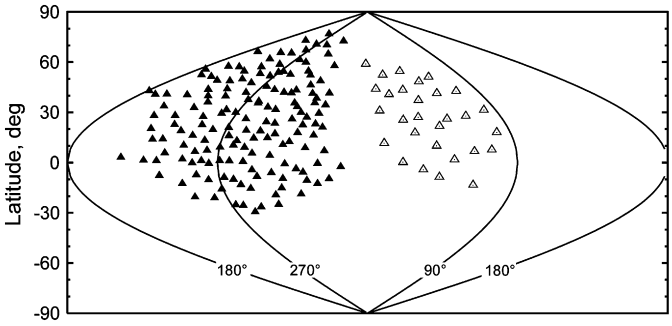

Fig. 1. Control-point locations on Iapetus (spherical latitude, longitude) in a sinusoidal map projection. Full/open triangles refer to points controlling the leading side/trailing side DTM. Due to lack of image overlap both control nets stand alone. For the leading side, the 1σ absolute point accuracies in the x, y, z coordinates amount to 1.1, 2.2, and 1.2 km, respectively, but for the trailing side this error is likely several kilometers because of uncertainties in fixing the limb (Giese et al., 2006a).

Table 1
Images of the leading side

Frame	Resolution [km]	Center		# ctrl
		East long. [deg]	Lat. [deg]	
N1482859953	4.3	290.3	6.4	25
N1483151512	1.1	299.3	4.5	94
N1483152827	1.1	263.9	55.0	93
N1483152937[a]	1.0	289.9	31.4	29
N1483153004[a]	1.0	290.0	31.5	22
W1483173621	8.7	294.8	38.2	18
N1483173746	0.9	282.7	39.9	100
N1483173841	0.9	309.2	−40.5	45
N1483174212[a]	0.9	296.3	42.3	29
N1483174398[a]	0.9	296.4	42.4	34
N1483194703[a]	0.8	309.8	55.2	37
N1483194883	1.1	267.7	11.1	59
N1483195224	1.2	333.6	−2.4	32
N1483195402	0.8	320.3	59.3	43
N1483195574	1.7	150.7	47.5	15

Resolutions refer to the center pixel of the frames. The last column shows the number of control points measured in the frame.
[a] For these frames, the center is outside of Iapetus. The given values refer to the sub-s/c point.

Table 2
Images of the trailing side

Frame	Resolution [km]	Center		# ctrl
		East long. [deg]	Lat. [deg]	
N1483212257	1.5	40.6	11.1	19
N1483224906	1.0	31.7	21.4	24
N1483236748	1.0	38.5	21.4	28
N1483247183	1.0	44.3	18.1	29
N1483280710	1.1	57.7	30.6	30

For the DTM of Iapetus' leading side, a control network of 154 points (Fig. 1) measured in 15 images (Table 1) was set up. For the smaller DTM of the trailing side we used 29 points measured in 5 images (Table 2).

3. Terrain models

Generally, our method of analysis allows computing both the topography and the global shape of a body from stereo image

data. Although we are primarily concerned with the topography of Iapetus, it is instructive to see what the global shape looks like from our approach. Fig. 2 (left) shows a terrain model when the ground points are referenced to a sphere (see Section 2). This reveals an extremely non-spherical shape of Iapetus consistent with the findings from global shape modeling, according to which Iapetus is best approximated by a $747.4 \pm 3.1 \times 712.4 \pm 2.0$ km oblate spheroid (Thomas et al., 2008).

But topography requires heights measured relative to an equipotential surface. At this place we adopt a geometrically defined reference surface given by the oblate spheroid axes above. This surface is not at equipotential level under current conditions of Iapetus' synchronous rotation but it likely was when Iapetus rotated at a period of ~16 h early in its history (Thomas et al., 2008). Most of Iapetus' surface features were inferred to be older than 4 Ga (Neukum et al., 2005) and are likely to have formed during the early fast rotating period [Ip (2006) has mentioned that damping of Iapetus' spin rotation is expected to occur in a long rather than short time scale]. Thus the chosen height reference is physically plausible. Minor deviations from the true equipotential surface will not change the relief of the features significantly. The terrain model with points referenced to the spheroid is shown in Fig. 2 (right). It is the basis for the subsequent analysis.

The terrain models of Iapetus' leading side were compiled from 12 individual stereo pairs with horizontal resolutions of 4–8 km and vertical accuracies of 300–800 m. The trailing-side DTM (Fig. 2, top) is a compilation from 2 stereo pairs with horizontal resolutions of 5–10 km and vertical accuracies of 200–400 m. Features smaller than or within these resolution limits are expected to be smoothed.

4. Topographic features

4.1. General topographic characteristics

4.1.1. Observations

Inspection of the DTM reveals that Iapetus' surface is dominated by impact-related topography. Craters are ubiquitous on Iapetus including large impact basins (Fig. 3). The largest impact basin (Fig. 2, 35° N, 272° E; Fig. 3, I) is about 800 km in diameter and has rim topography of up to 10 km extending over scales of some hundreds of km (Fig. 2, bottom profile). The rim-to-bottom relief is 14 km at maximum. Another topographic landform is the equatorial ridge, which is tens of kilometers wide with heights of up to 13 km (see crosses in Fig. 2) within the modeled area (limb profiles show relief up to 20 km elsewhere, Fig. 5, top). The stratigraphic relationships suggest that both the 800 km basin and the equatorial ridge belong to the oldest features with likely ages of 4.4–4.5 Ga (Neukum et al., 2005).

The lowest points within the modeled area have heights down to about −10 km and are found at the bottoms of basins VI and VII (Fig. 3).

4.1.2. Implications

Thomas et al. (2008) have computed residual limb topography on Iapetus and on the other icy Saturn satellites. This has shown that Iapetus is exceptional in its large surface relief. Our contiguous terrain model now confirms these findings. Moreover, Iapetus' topography can be compared with topography obtained for Tethys (Giese et al., 2006b) and with Voyager-based elevation models of large impact features on the middle-sized icy satellites (Moore et al., 2004a). All of these show lower height ranges than exhibited by Iapetus.

Obviously, Iapetus has retained much of its impact-related topography and the (old) ridge topography. This implies a thick lithosphere at the time of formation to support the associated loads. If it were the case that Iapetus is not homogeneous, density contrasts are expected to be of minor importance in supporting topography because Iapetus' low density (1.08 g/cm^3, Thomas et al., 2008) implies only a small rock mass ratio. The thickness of the lithosphere can be estimated from models of lithospheric deflection by imposed surface loads (Brotchie and Silvester, 1969). Here, we solve for a lithosphere thick enough to prevent subsiding of the observed rim loads of the 800 km basin. The underlying assumption is that this topography has not suffered a significant height loss by lithospheric deflection. Measurements of a rim-height dependence on crater diameter would allow identification of rim topography subsidence but such measurements do not exist yet. An empirical relation for complex lunar craters (Pike, 1977) predicts a rim height of 3.4 km for an 800-km crater which is much lower than the observed rim heights and thus may support the assumption. As a model load for lithospheric deflection, we considered a segment of rim topography. To simplify the problem, we approximated the load represented by the rim profile by a disc-shaped load with the same force (Fig. 4). Deflection profiles were then computed on the basis of equations given in Appendix A. These reveal that lithospheric thicknesses of 100–125 km are required to prevent more than 1 km of subsidence of the load. For the deflections to be less than 2 km lithospheric thicknesses of 40–60 km are required. Larger deflections are unlikely to have occurred because this would have formed a pronounced depression on the spherical shell in the surroundings of the load which is not observed. From this we conclude that likely lithospheric thicknesses more than 4 Ga ago range from 50–100 km.

4.2. The equatorial ridge

4.2.1. Observations

A set of profiles across the ridge (Fig. 5) shows that the morphology changes along the equator. The top profiles r2–r5 display a trapezoidal shape up to 70 km wide with upper flanking slopes of typically 15°, and a pronounced plateau. However, the higher resolution anaglyph image (Fig. 3) reveals that the plateau actually has finer-scale topography consisting of an inner ridge aligned with two outer ridges of about the same height and narrow gaps in between. Profiles r3 and r4 indicate a distinct change in their north-facing flanking slopes from 15° to 8° and 4°, respectively. This is also seen in the anaglyph image (e.g., the dashed profile). Moreover, the anaglyph image reveals

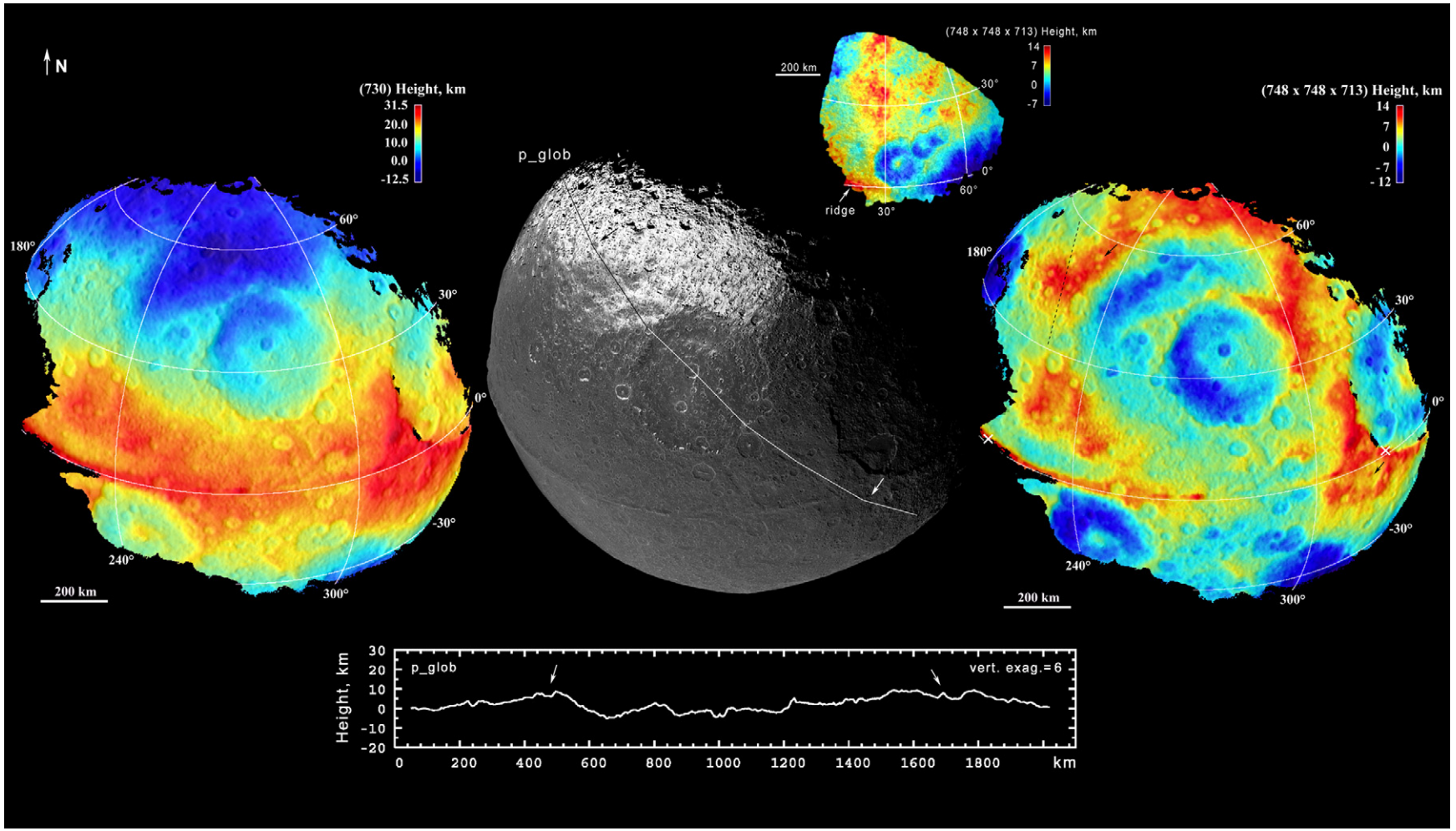

Fig. 2. Color-coded topography of Iapetus in orthographic projection. (Left) Iapetus' leading side with heights referenced to a sphere (radius = 730 km). (Right) Iapetus' leading side with heights referenced to an oblate spheroid (Thomas et al., 2008). This strongly reduces the height range of the model and reveals detail not recognized before. The dashed line marks a profile used for modeling the lithospheric load (Fig. 4). White crosses mark the locations of the points with the largest heights of ∼13 km. Projection center is at 30° N, 270° E for both models. (Center) Image mosaic compiled from raw (not map projected) images. The line indicates the location of the profile (with heights referenced to the oblate spheroid) shown below. (Top) Iapetus' trailing side topography. Projection center is at 30° N, 30° E.

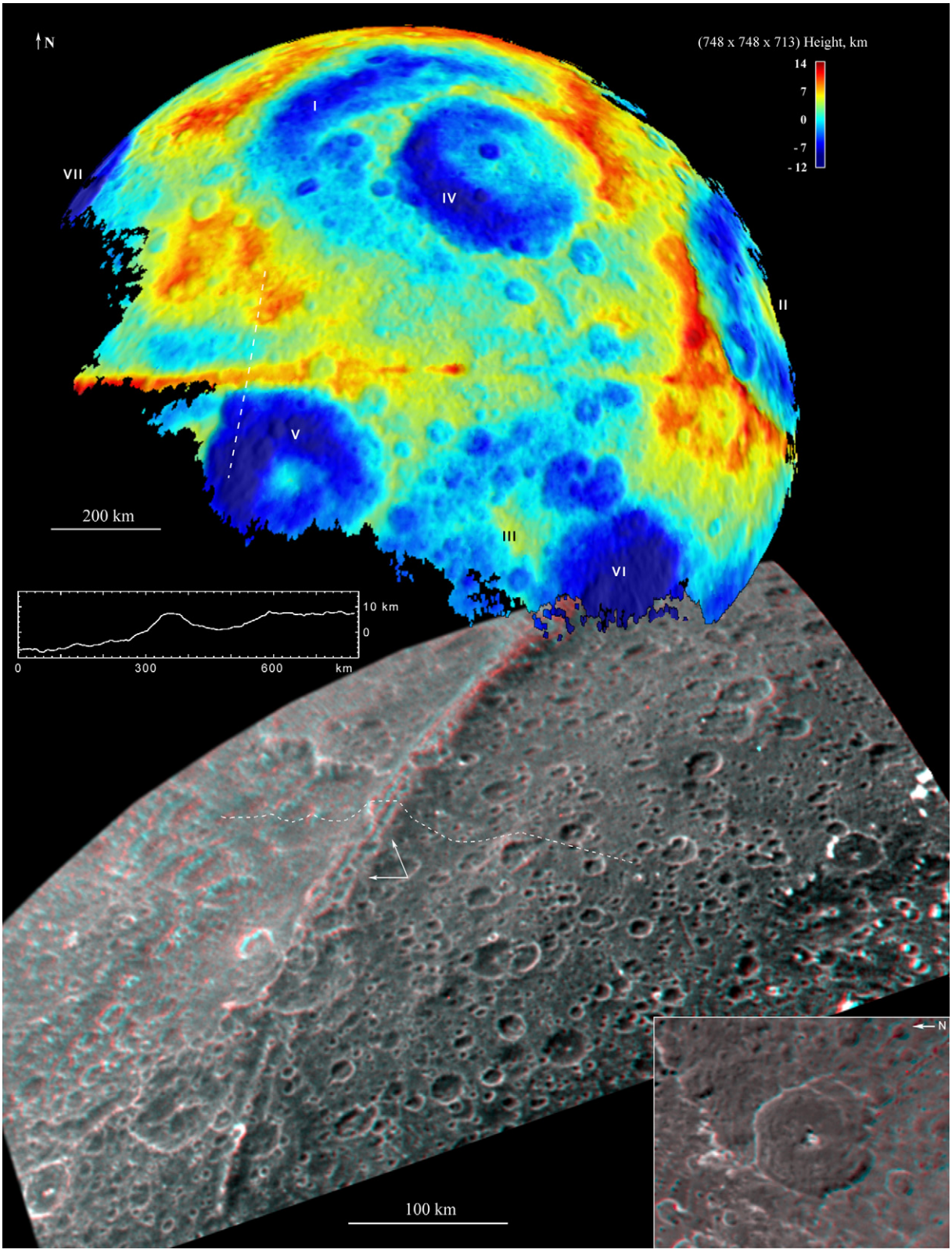

Fig. 3. (Top) Color-coded DTM (centered at 7° S, 263° E) showing the locations of large basins. The largest and smallest basins (labeled I and VII) have diameters of 800 and 340 km, respectively. (Bottom) Anaglyph images (red: left, blue: right) showing the morphology of the equatorial ridge and of an 80-km central-peak crater (profiled by c8 in Fig. 9), respectively. Used frames: N1483174398, N1483152937; N1483194883, N1483173746. Arrows point to locations where the (rising) ridge has pushed away surface material. (Center) Profile taken along the dashed line above (see also r4 of Fig. 5). The approximate location in the anaglyph image is also marked by a dashed line.

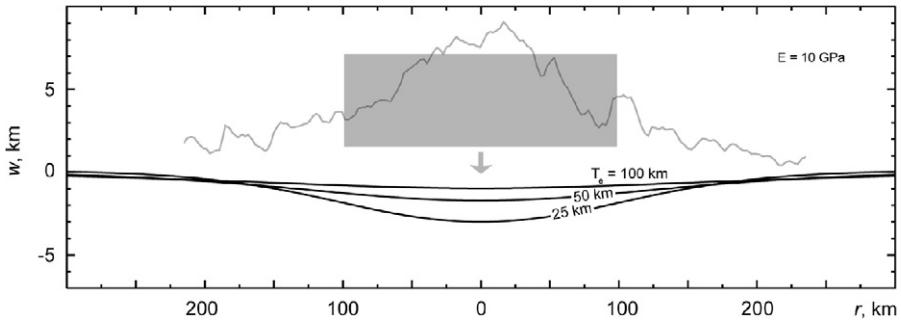

Fig. 4. Deflection w of the lithosphere as a function of radial distance r from the load (see Appendix A). For the purpose of modeling, the 8 km high load represented by the profile above (see Fig. 2 (right), dashed line) is replaced by a disc-shaped load exerting the same force. A lithosphere only 25 km thick is subject to a large deflection of 3 km but a lithosphere 100 km thick would be subject to a deflection smaller than 1 km for a Young's modulus (E) of 10 GPa. A weaker lithosphere with $E = 1$ GPa must be 125 km thick to prevent deflections larger than 1 km.

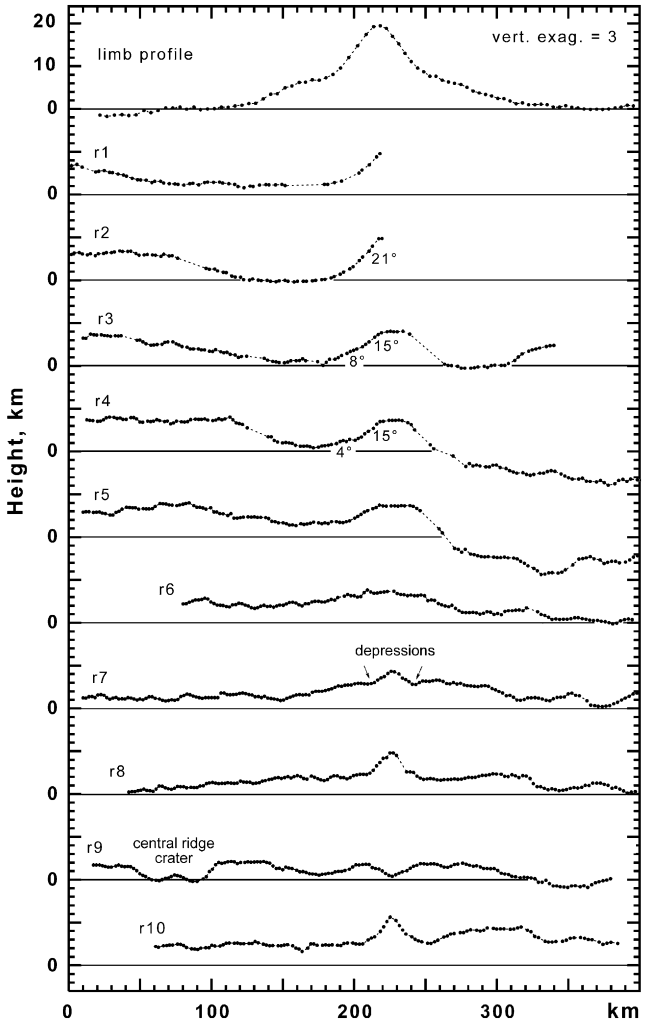

Fig. 5. Profiles across the equatorial ridge. Profile locations are shown in Fig. 6. The top profile is a section of limb profile N1482859953 (Thomas et al., 2008) showing ridge heights in a location distant from the area covered by the DTM.

that the pre-existing upper surface layer rose up along the flank of the ridge as it formed (arrows point to such places). There is a 100-km-wide depression with a sharp boundary north of the ridge and aligned with it (Fig. 2, longitudes <250° E). A similar southern depression may also exist as indicated by the DTM. Profile r7 marks a change in ridge shape. At this place the ridge is made up of the inner ridge only, which exhibits a triangular shape there, but the outer ridges are at lower heights and less pronounced. The narrow gaps as observed above have become wider and form small depressions on both sides of the inner ridge (r7). Further away (r9) the ridge appears as a faint feature at the bottom of a 40-km-broad depression (see inset in Fig. 6), but along to the east (r10) it again appears as a triangular high-standing feature.

While the largest ridge heights reach 13 km within the DTM (Fig. 2) shape modeling has provided heights of up to 20 km in other places along the equator (Fig. 5, limb profile).

The trailing side DTM (Fig. 2, top) reveals that the ridge continues on this hemisphere.

4.2.2. Implications

The formation of the ridge is still an unresolved problem. Currently, there are two different theories. Porco et al. (2005) suggested an origin related to the overall shape or changes in spin state of Iapetus but they also noted that the ridge does not show characteristics or patterns comparable to the tectonic pattern seen in despinning models. In addition to this, Ip (2006) pointed out problems related to the old age of the ridge on the one hand and predicted long despinning time scales of Iapetus on the other hand. To avoid that problem among others, he suggested an exogenic origin where the ridge was formed by collisional accretion of a ring remnant. This theory invokes a ring remnant steming from the formation of the proto-Iapetus, and a thick atmosphere to force the ring particles drifting towards the surface.

Our observations here argue for an endogenous origin of the ridge. The ridge's appearance is consistent with it having been formed by material rising from below, which thereby upwarped the surface on both sides. This is primarily suggested by the different slopes measured at the ridge flanks (r3, r4). The lower slopes are much less than the angle of repose and thus are potentially related to upwarping of the surface but the upper, steeper slopes are related to the rising material within this formational model. The observed broad depressions aligned with the ridge for longitudes <250° E (Fig. 2) may consequently be of flexural origin. If the ridge were to consist of piles of ring material slopes close to the angle of repose would be expected but this is not observed.

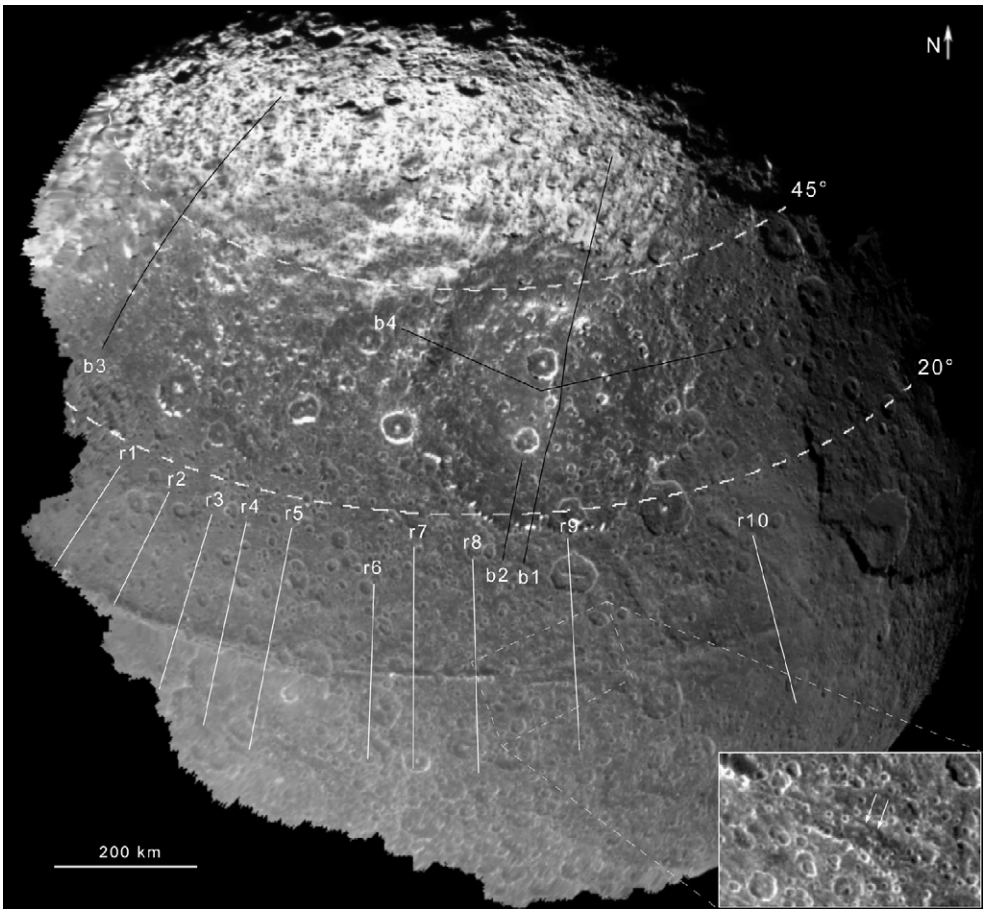

Fig. 6. Location of ridge profiles (r1–r10) and profiles (b1–b3) showing the relation between image brightness and topography (Fig. 7). Arrows in the inset mark a location where the inner ridge is in a depression but still intact.

The absence of the ridge in some places is clearly the result of impact erosion but in other places, e.g., the depression profiled by r9, it may be related to a more complex formational process than described above. Likewise, the change in the ridge shape from trapezoidal to triangular along the equator hints at a complex process. On the other hand, post-formational tectonic processes may have modified the shape of the ridge which could also explain the rather complex morphology.

A flat-topped ridge with sharp edges in places is hard to explain by Ip's theory, as is the fact that the ridge has upwarped the adjoining surface. Overall, the structure of the ridge is too complex to have been formed simply by deposition of putative ring particles.

4.3. Dark and bright terrains in relation to topography

Iapetus is well known for its albedo dichotomy between the leading side and the trailing side (Smith et al., 1981, 1982). The leading-side material is an order of magnitude darker than that on the trailing side and was suggested to be of exogenic origin (Vilas et al., 2004; Buratti et al., 2005). But high-resolution Cassini imaging has revealed that the leading side is not entirely dark. Here, we study the distribution of bright and dark terrains on the leading side in relation to topography. A detailed discussion on the albedo dichotomy is given in a companion paper (Denk et al., in preparation).

4.3.1. Observations

Fig. 6 shows that northern latitudes $\geqslant 45°$ are dominated by bright terrains and equatorial latitudes $\leqslant 20°$ are predominantly dark. But bright areas are found at low ($\sim 20°$) latitudes if slopes are north facing and steep (Fig. 7, compare topography and image brightness of the crater wall along b1: 29° slope with neighboring b2: 6° slope; b3: crater 1 & 2). Likewise, dark areas are found at high northern latitudes ($\sim 50°$) if slopes are south facing (Fig. 7, b3: depression). East facing slopes, although as steep as the north facing slope, are dark (Fig. 7, compare b1 with b4). Dark material is preferentially collecting in topographic lows, e.g., at the bottom of craters (Fig. 8).

4.3.2. Implications

To darken the leading side of Iapetus solely from exogenic sources by an order of magnitude as compared to the trailing side would require unrealistically large amounts of dark material. Thus, a purely exogenic origin is unlikely (Denk et al., in preparation). Consistent with this hypothesis, our observations suggest that image brightness on Iapetus' leading side is controlled by sublimation with the dark material being a lag deposit originating from a bright icy substrate mixed with dark

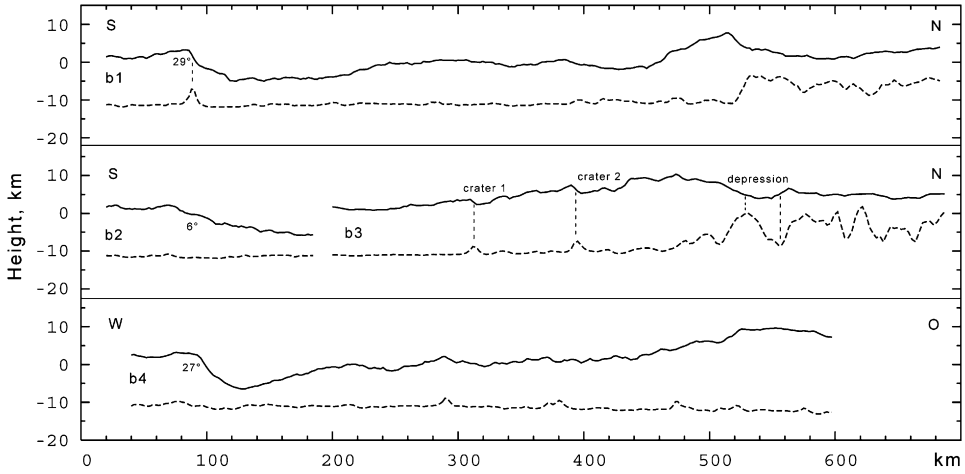

Fig. 7. Topography (solid lines) in relation to image brightness smoothed to the DTM's resolution (dashed lines). Profile locations are shown in Fig. 6. Vertical exaggeration of topography is 3, image brightness is scaled by a factor of 1/15.

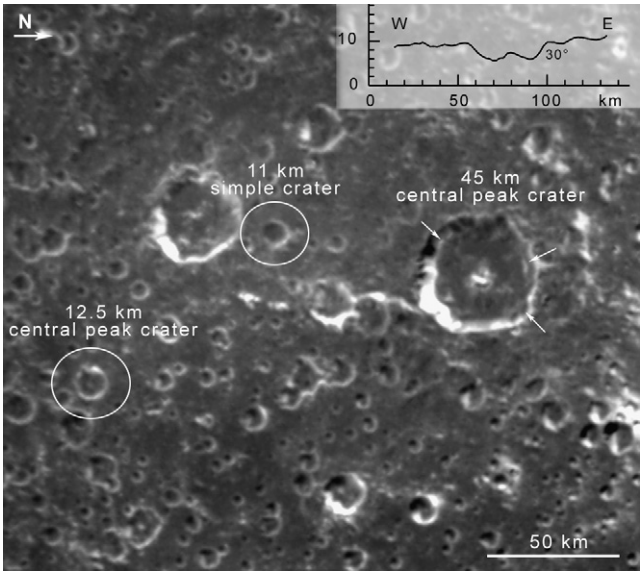

Fig. 8. Cut out of frame N1483194883 showing dark deposits in a 45-km crater. The Sun illuminates the surface from the upper left. The dark material at the crater bottom is interpreted as a sublimation lag deposit originating in parts from down-slope movement of dark, sublimation-related material from the upper rimwall. The upper rimwall of the crater has a terrace (visible in these image data (arrows) and revealed by c3c of Fig. 9 but otherwise not resolved by the DTM) and associated with this, an upper rimwall slope likely steeper than the angle of repose (Melosh, 1989). The upper north-facing rimwall appears bright, which we interpret as lack of sublimation due to insufficient solar radiation. The west-facing rimwall appears brighter than the east facing one likely because of its higher steepness (compare profile). Dark material originating there may move completely down-slope leaving behind a high-albedo surface and thus, leading to lower sublimation in this place. Encircled features mark craters at the transition from simple to complex central peak morphologies, which occurs at diameters of about 11 km for Iapetus.

components. The degree of darkening of the surface is determined by the incident solar radiation which depends on latitude and slopes (steepness and orientation), but also important is the down-slope movement of the dark lag deposit from steep slopes, which leaves behind a brighter surface and leads to dark deposits in topographic lows (Fig. 8). A very similar process has been proposed for the landscape evolution of Callisto, where it is discussed in detail by Moore et al. (1999, 2004b). Frost deposits are also consistent with the observations and may have contributed significantly to surface brightness at higher latitudes (Spencer et al., 2005).

4.4. Craters

There has been extensive work on crater formation on icy satellites based on Voyager images, and on differences to the terrestrial planets (e.g., Chapman and McKinnon, 1986; Schenk, 1989, 1991). Iapetus was not included in the analysis so far because of poor image resolutions but there exists valuable information on crater morphologies for Iapetus from similarly-sized Rhea, which was imaged by Voyager at resolutions even better than the Cassini Iapetus data. Here, we report on crater morphologies of Iapetus and compare these with morphologies obtained for craters of Rhea (Moore et al., 1985; Schenk, 1989, 1991). However, it has to be noted that as opposed to the morphologic data from our DTM the Rhea data are based on methods of photoclinometry and shadow length measurements, which can introduce a priori discrepancies in the results (Jankowski and Squyres, 1991).

4.4.1. Observations

There are four, morphologically different crater types on Iapetus' leading side. In the terminology of Wood and Head (1976) these are (in progression from smallest to largest) simple craters, central peak craters, central peak basins and peak-ring basins. Simple craters are below the DTM's resolution and not considered here, instead we focus on the larger complex craters with diameters >25 km.

Central peak craters: The transition from simple to complex central peak craters occurs at diameters of 11 ± 3 km (an example is shown in Fig. 8) consistent with predictions of <49 km for Iapetus (Schenk, 1989) and similar to values of 15 ± 5 km found for Rhea (Chapman and McKinnon, 1986). The morphology of selected central peak craters is shown in Fig. 9. These craters exhibit conically shaped central peaks with typical flanking slopes of 11° covering a portion of 0.3–0.5 of the

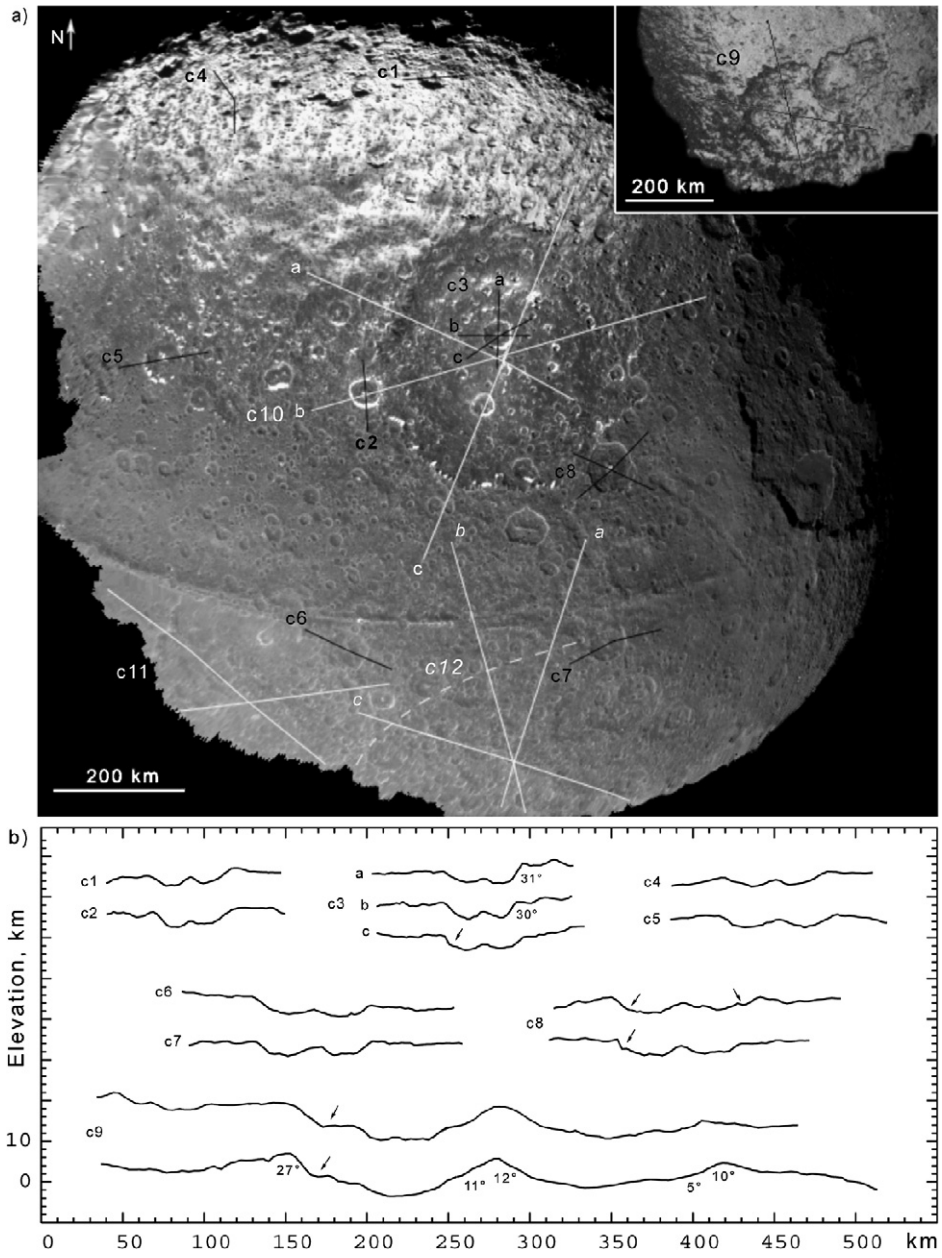

Fig. 9. Topographic profiles showing the morphology of central peak craters (c1–c9). Central peaks are conically shaped with typical flanking slopes of ∼11°. Some craters show indications of rimwall terracing (arrows). More evidence for terracing is in the higher-resolution image data (for c3 compare with Fig. 8; for c8 compare with Fig. 3—the 80 km crater). Flat floors exist in some cases but are not very pronounced. Vertical exaggeration of topography is 2.5.

craters' diameters (D) (Fig. 11a). Peak widths found for Rhea range from 0.3–0.4D (Schenk, 1991). There is indication of flat floors in some cases (Fig. 9, c1, c2, c7) but not as pronounced as for craters, e.g., on the Moon, which have narrower peaks of ∼0.2D (Schenk, 1991). Central peak heights (Fig. 11b) increase with crater diameter until an inflection point in slope at $D \sim 300$ km is reached. Peak heights can rise above the surrounding planes (Fig. 9, c9). Peak heights of craters on Iapetus seem to be systematically lower than on Rhea, e.g., at a diameter of 40 km, peak heights on Iapetus range from 0.6–1.0 km, but on Rhea this is 1.3–2.0 km (Fig. 8a in Schenk, 1991). However, this discrepancy may be related to the different methods applied to infer topographic information. While there is a tendency to smooth small-scale (<10 km) features of the peaks within our method of analysis (Section 3), Schenk (1991) mentioned that slopes derived from photoclinometry are probably overestimated, and it is very likely that the peak heights determined by this method are as well (most of the peak heights for Rhea were from photoclinometry). Likewise, crater depths increase with diameter until $D \sim 300$ km above which crater depths are lower than predicted by the trend line (Fig. 11c). Crater depths seem to be systematically lower on Iapetus than on Rhea; however, this offset is within the error bars of the shadow-length measurements (even with inverse gravity-scaling (Schenk, 1991) taken into account), although not for the photoclinometry data (likely for the same reason as noted for

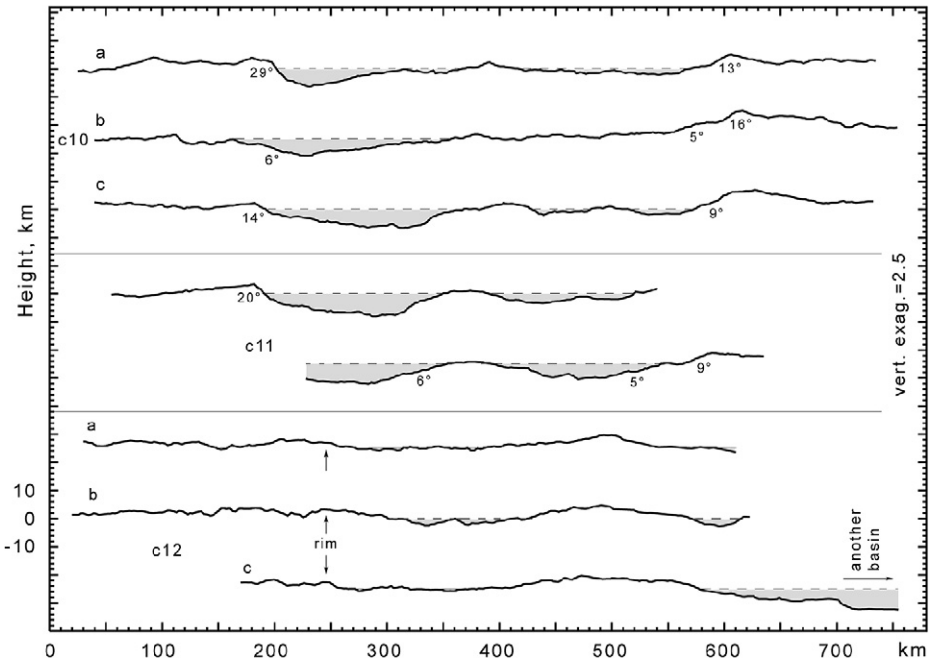

Fig. 10. Topographic profiles showing the morphology of central peak basins (c10–c12). The profiles' locations are given in Fig. 9. While central peak craters have pronounced conically shaped peaks in their centers central peak basins have broader, less tapered peaks with lower slopes. Rimwall slumping is prominent in these craters. The rim of the basin profiled in c12 is marked by a dashed line in Fig. 9.

peak heights above). Rimwall slopes as indicated by the topographic data reach values of up to 31° (Fig. 9, c3a) but may be steeper still when measured over scales <10 km. Rimwall slumping and associated terracing is observed in the topographies of several craters down to a diameter of 45 km (Figs. 8, 9) but visual inspection of the image data suggests that there are more 40–80 km craters exhibiting rimwall slumping, which is not resolved by the DTM. For Rhea, Schenk (1989) found only a few craters with possible terracing, the smallest one with a diameter of 80 km. He introduced an inflection point in the crater depth-to-diameter measurements at the onset of rimwall slumping (following the inflection point at the onset of central peaks) but this is not observed in our data (Fig. 11c). Generally, rimwall slumping was found to be relatively unimportant in complex craters on icy satellites (Schenk, 1989). A well resolved terrace structure with a width of ∼12 km is seen in a 277 km crater profiled by c9 of Fig. 9.

Central peak basins: Central peak basin morphologies are shown in Fig. 10. The basins exhibit broader, less tapered peaks and rimwall slumping with average slopes of 5°–10° (c10, c11), but individual slopes associated with terracing (Fig. 7, b1) are as steep as 29°. There is a 500 km basin (Fig. 10, c12) that is heavily degraded as compared to the other basins and hence must be the oldest among the basins identified here. This basin has little relief (relative to the other basins) and can only be discerned by its topographic outline (Fig. 3, basin III). Central peak heights and depths (Figs. 11b, 11c) indicate a characteristic change in slope associated with the basins. Basin IV does not show a pronounced peak overall, rather the crater floor is a broad, shallowly sloped convex feature (Fig. 10, c10a, b). No outer rings are observed around the basins.

Peak-ring basin: A 590 km basin with a potential peak-ring complex is shown in Fig. 12. The inner ring diameter is nearly half of the basin's diameter. Peak width, height, and crater depth are consistent with the values of neighboring central peak basins (Fig. 11).

A single central-ridge crater is shown in Fig. 13. More craters of that type were not observed. Central-ridge craters are also exceptions on Rhea (Schenk, 1991). The crater is elongated along ridge strike. The ridge is triangular in cross-section and exhibits topographic maxima at its ends. In contrast to other similar-sized craters which exhibit terracing on the rimwall this crater does not.

4.4.2. Implications

The observed inflection point in central peak heights and crater depths at diameters of ∼300 km is interpreted as onset of crater relaxation due to viscous flow of ice at depth. While craters with $D < 300$ km have completely formed in the (cold) lithosphere, the larger craters have probed the astenosphere and thus have experienced relaxation of the crater floor. However, the excavation depth which is only a fraction of the transient crater depth must still have been smaller than the thickness of the lithosphere because otherwise outer rings should have formed (McKinnon and Melosh, 1980). Using relations between the excavation depth (H_{exc}) and final crater diameter (D) for craters on the terrestrial planets (Melosh, 1989)

$$H_{\mathrm{exc}} \sim 1/10 D_t \quad \text{and} \quad D_t \sim 1/2.7 D, \tag{1}$$

where D_t is the transient crater diameter, an estimate of the excavation depths for the basins can be obtained. As an upper limit, Eq. (1) provides a value of ∼30 km at a diameter of 800 km. This is less than lithospheric thicknesses of 50–

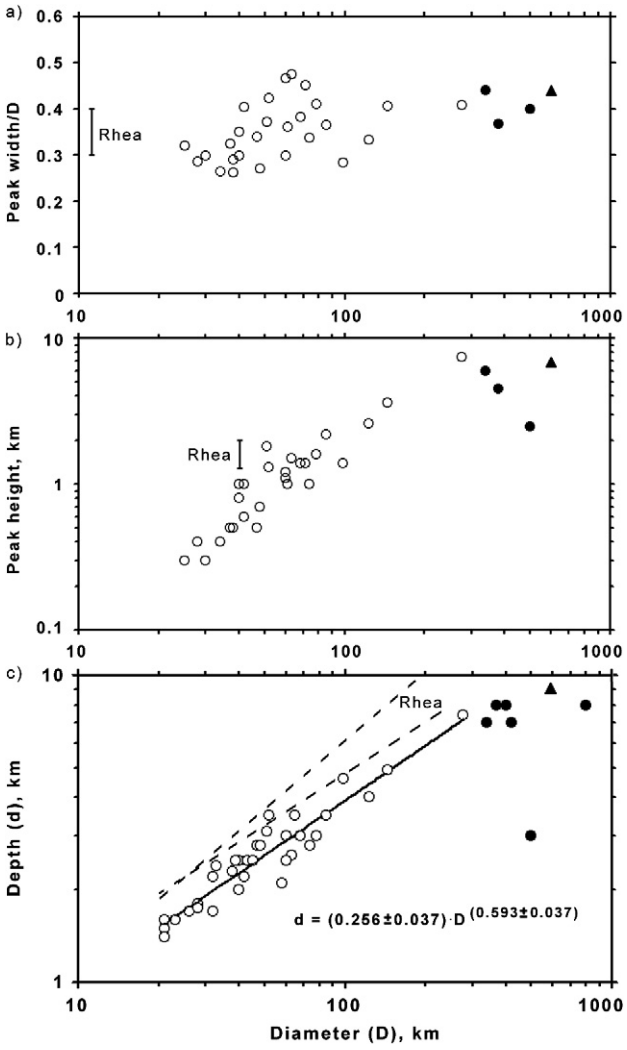

Fig. 11. (a) Widths and (b) heights of central peaks of complex craters as functions of crater diameter. Open circles mark central peak craters, solid circles mark central peak basins, solid triangle marks a potential peak-ring basin shown in Fig. 12. Peak widths are similar to those found for Rhea, but peak heights seem to be systematically lower on Iapetus. (c) Crater depth as function of diameter. The solid line is a least-squares fit to the data of central peak craters. For Rhea, corresponding fits are $d = 0.209(+0.075, -0.054)D^{0.734\pm0.104}$ (from photoclinometry, upper dashed line) and $d = 0.366(+0.230, -0.141) \times D^{0.559\pm0.163}$ (from shadow length measurements, lower dashed line), respectively (Schenk, 1989). As for peak heights, crater depths are systematically lower on Iapetus than on Rhea. This discrepancy becomes still larger if gravity-scaling is applied to these data. There is an inflection point in slope at diameters of ~300 km both for peak heights and crater depths.

100 km found in Section 4.1 and therefore consistent with the lack of outer rings as observed. All basins seem to have experienced viscous relaxation, notably the 500 km basin (Fig. 10, c12), which has lost about 7 km of depth by this process when measured with respect to the trend line (Fig. 11c). This basin presumably formed prior to all other basins at a time when the lithosphere was thinner and hence relaxation was most rapid. The relaxation-related relative basin age inferred here from topography is consistent with the degradation-related relative age inferred from the degree of impact erosion. Basin IV shows indication of a doomed floor which is suggestive for having formed by viscous relaxation (Parmentier and Head, 1981).

Complex crater formation has been described within a Bingham rheologic model, which incorporates both a viscous fluid behavior characterized by a viscosity η and a perfectly plastic behavior characterized by an effective cohesion c of the material wherein a crater is formed (Melosh, 1989). Specifically, crater collapse associated with slope failure occurs when

$$\frac{\rho \cdot g \cdot d_t}{c} \geqslant 5, \tag{2}$$

where ρ is the density, g is gravity, and d_t is the depth of the crater at the onset of slope failure. This equation can be used to estimate the cohesion of the shocked icy material when the depth is known. Here, we assume a depth of 1.1 km, which corresponds (when the trend line equation of Fig. 11c is applied) to a failure onset diameter of 11 km equal to the onset diameter for central peaks. Using values of Iapetus' density and gravity as given in Appendix A, Eq. (2) results in a cohesion of 0.05 MPa. An alternative approach to estimate the cohesion is to use the predicted width w of individual terraces resulting from crater collapse. This is given by (Melosh, 1989)

$$w = \frac{c}{\rho \cdot g} \cdot \left(\frac{1 + 16\lambda^2}{16\lambda^2}\right), \tag{3}$$

where λ is the depth/diameter ratio of the crater at the time when the terrace forms. The widest and best defined terrace occurs just below the crater rim. It is the last terrace to form, when λ is only slightly larger than its final value. For lunar craters, widths of the largest terrace increase with crater diameter reaching $w = 14$ km when extrapolated to diameters of 270 km (Melosh, 1989, Fig. 8.15). The crater profiled by c9 in Fig. 9 has a diameter of 277 km and a terrace width of $w = 12$ km similar to the lunar value. Applying Eq. (3) to that crater (note that at the time the terrace formed D was equal to 277 km $- 2w$; crater depth = 7.4 km) a cohesion of 0.04 MPa is obtained which is consistent with the above estimate, and of the same order as estimates of 0.06 MPa obtained for Rhea (Schenk, 1989). Once collapse is initiated, the material behaves as a fluid forming a central peak if the viscosity is less than a critical viscosity given by (Melosh, 1989)

$$\eta_{\text{crit}} \sim \rho \cdot g^{1/2} \cdot D^{3/2}, \tag{4}$$

where D has to be taken at the onset of central peak formation. Using $D = 11 \pm 3$ km for Iapetus a viscosity of 0.6 ± 0.2 GPa s is obtained. For Rhea, with an onset diameter of 15 km, the viscosity is somewhat larger.

Slopes close to 30°, as are measured in upper rim locations of some craters here are typical for scarps just below the crater rim in fresh lunar craters, which commonly stand at slopes of 30°, near the angle of repose. Average rimwall slopes of the larger complex craters on Iapetus are similar to average slopes of the terrace zones in complex lunar craters which are between 7° and 14° (Melosh, 1989). Such slopes are far below the normal angle of repose and can be explained to form when the material beneath a collapsing crater has a plastic yield strength rather than strength related to frictional sliding.

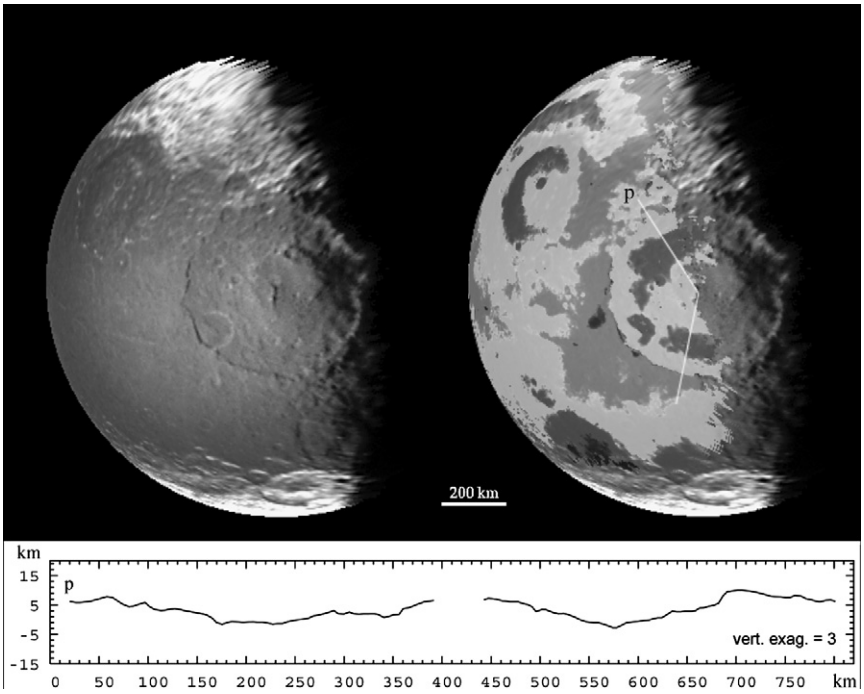

Fig. 12. Image showing a potential peak ring complex in a 590 km basin on Iapetus. The ratio of the inner ring diameter to the rim diameter is 0.44. (Left) Frame N1482859953 in orthographic map projection and with superimposed black-and-white-coded DTM heights (right).

Peak-ring basins have been tentatively identified on the icy satellites of Saturn so far (Moore et al., 2004a; Stooke, 2002). On the terrestrial planets, they exhibit inner-ring diameters typically half of the basin's diameter (Melosh, 1989). The observed peak-ring diameter thus is consistent with the formation of a peak-ring basin in the present case. Peak-ring complexes are thought to form when the central uplift itself collapses after an initial rise (e.g., Collins et al., 2002). For lunar craters, this collapse occurs at crater diameters larger than 140 km (Melosh, 1989), for Iapetus, the onset of peak-ring basin formation seems to occur at diameters of 500–600 km. Applying inverse gravity-scaling to the collapse diameter on the Moon provides an onset diameter of ~1000 km for Iapetus. This is substantially larger than the observed range and consistent with lower (strength versus gravity) transition diameters predicted for ice as compared to hard rock (Chapman and McKinnon, 1986). The 800-km basin may also have had a peak ring, but if this feature once existed it was erased by a subsequent impact, which formed basin IV (Fig. 3).

Central-ridge craters appear to be a special form of central peak craters. Their morphology suggests that they likely form by closely spaced projectiles of about the same mass and velocity which produce individual central peaks that merge in a final central ridge with topographic highs at the ends. More separated projectiles produce double craters (Fig. 13, inset). Alternatively, central-ridge craters might have formed by very oblique impacts as is suggested by the elongated along ridge strike crater shape.

A rim-slumping transition diameter cannot be resolved by our depth-to-diameter measurements (Fig. 11c) but it is plausible that it occurs at diameters <45 km. As rimwall slumping widens the crater and as there seems to be less evidence for rimwall slumping on Rhea, this may account for the relative shallowness of craters on Iapetus as compared to Rhea.

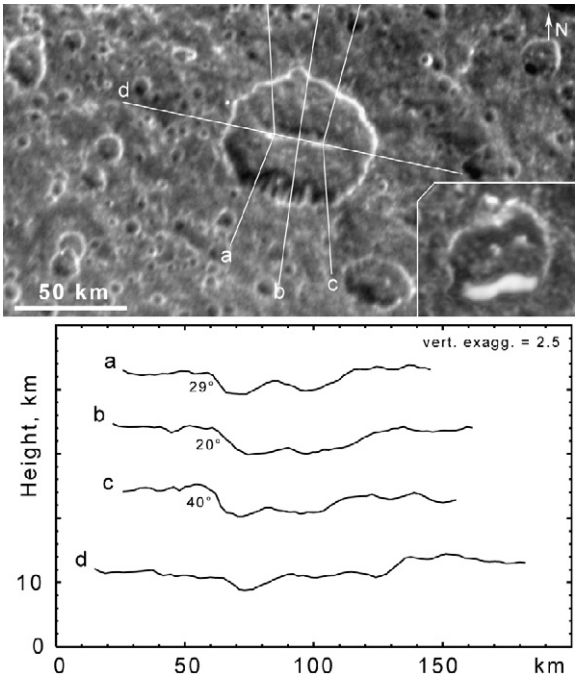

Fig. 13. Morphology of a 50 × 70 km central ridge crater. The crater is elongated along ridge strike, and the ridge exhibits maximums at its ends. It may have formed by two, closely spaced projectiles. Inset shows a double crater which might have been formed by two widely separated projectiles. Image data are cut outs of frame N1483194883.

5. Summary

Iapetus' large topography is exceptional among the middle-sized icy Saturn satellites and implies a lithosphere as thick as 50–100 km early (~4.5 Ga) in its history.

Iapetus' prominent equatorial ridge shows morphology consistent with an endogenous origin.

Albedo on Iapetus' leading side is controlled by sublimation with the dark material being a lag deposit originating from a bright icy substrate mixed with dark components.

The transition from simple to complex central peak craters occurs at diameters of 11 ± 3 km. The morphology of central peak craters on Iapetus resembles morphologies of craters on similarly sized Rhea. A prominent difference however is that craters on Iapetus seem to be shallower (although, it cannot be excluded that this feature is related to the different methods applied to infer the crater topographies) and show more pronounced rimwall slumping, which would explain the relative shallowness. Impact basins with diameters $\geqslant$300 km show strong evidence for viscous relaxation. The effective cohesion and viscosity of shocked icy material was estimated at 0.04 ± 0.01 MPa and 0.6 ± 0.2 GPa s, respectively.

Appendix A

Brotchie and Silvester (1969) showed that the deflection w of an elastic, thin, spherical shell by a disc-shaped load of radius R_d and height h is given by

$$w = h \cdot \left[s \cdot \mathrm{ker}'(s) \cdot \mathrm{ber}(x) - s \cdot \mathrm{kei}'(s) \cdot \mathrm{bei}(x) + 1 \right] \quad \text{for } x < s$$

and

$$w = h \cdot \left[s \cdot \mathrm{ker}(x) \cdot \mathrm{ber}'(s) - s \cdot \mathrm{kei}(x) \cdot \mathrm{bei}'(s) + 1 \right] \quad \text{for } x > s$$

with $x = \frac{r}{\beta}$, $s = \frac{R_d}{\beta}$, and $\beta = [\frac{D}{\rho \cdot g}]^{1/4}$, where r is the radial distance from the load, ρ denotes the density, g denotes gravity, and $D = \frac{E \cdot T_e^3}{12 \cdot (1-\nu^2)}$ is the flexural rigidity given by Young's modulus E, the effective elastic thickness T_e and the Poisson ratio ν. ker, kei, ber, and bei are Bessel–Kelvin functions of zero order.

In the modeling, we used $g = 0.222$ m/s^2, $\rho = 1.083$ g/cm^3 (Thomas et al., 2008) and $\nu = 0.33$.

References

Brotchie, J.F., Silvester, R., 1969. On crustal flexure. J. Geophys. Res. 74, 22, 5240–5252.

Buratti, B.J., Hicks, M.D., Davies, A., 2005. Spectrophotometry of the small satellites of Saturn and their relationship to Iapetus, Phoebe, and Hyperion. Icarus 175, 490–495.

Chapman, C.R., McKinnon, W.B., 1986. Cratering of planetary satellites. In: Burns, J.A., Matthews, M.S. (Eds.), Satellites. Univ. of Arizona Press, Tucson, pp. 492–580.

Collins, G.C., Melosh, H.J., Morgan, J.V., Warner, M.R., 2002. Hydrocode simulations of Chicxulub crater collapse and peak-ring formation. Icarus 157, 24–33.

Croft, S.K., 1991. Iapetus: Tectonic structure and geologic history. In: NASA Technical Memorandum 4300, Reports of Planetary Geology and Geophysics Program-1990. NASA Office of Space Science and Applications, Washington, DC, pp. 101–103.

Denk, T., Matz, K.-D., Roatsch, T., Wolf, U., Wagner, R., Neukum, G., Jaumann, R., 2000. Iapetus (1): Size, topography, surface structures, craters. Lunar Planet. Sci. XXXI. Abstract 1596.

Giese, B., Oberst, J., Roatsch, T., Neukum, G., Head, J.W., Pappalardo, R.T., 1998. The local topography of Uruk Sulcus and Galileo Regio obtained from stereo images. Icarus 135, 303–316.

Giese, B., Neukum, G., Roatsch, T., Denk, T., Porco, C.C., 2006a. Topographic modeling of Phoebe using Cassini images. Planet. Space Sci. 54, 1156–1166.

Giese, B., Wagner, R., Neukum, G., Helfenstein, P., Porco, C.C., 2006b. Topographic features of Ithaca Chasma, Tethys. Lunar Planet. Sci. XXXV. Abstract 1749.

Ip, W.-H., 2006. On a ring origin of the equatorial ridge of Iapetus. Geophys. Res. Lett. 33, doi:10.1029/2005GL025386. L16203.

Jankowski, D.G., Squyres, S.W., 1991. Sources of error in planetary photoclinometry. J. Geophys. Res. 96, 20907–20922.

McKinnon, W.B., Melosh, H.J., 1980. Evolution of planetary lithospheres: Evidence from multiringed structures on Ganymede and Callisto. Icarus 44, 454–471.

Melosh, H.J., 1989. Impact Cratering. Oxford Univ. Press, New York.

Moore, J.M., Horner, V.M., Greeley, R., 1985. The geomorphology of Rhea. J. Geophys. Res. 90 (suppl.), C785–C795.

Moore, Jeffrey M., and 13 colleagues, 1999. Mass movement and landform degradation on the icy Galilean satellites: Results of the Galileo Nominal Mission. Icarus 140, 294–312.

Moore, J.M., Schenk, P.M., Bruesch, L.S., Asphaug, E., McKinnon, W.B., 2004a. Large impact features on middle-sized icy satellites. Icarus 171, 421–443.

Moore, J.M., and 11 colleagues, 2004b. Callisto. In: Bagenal, F. (Ed.), Jupiter. Cambridge Univ. Press, Cambridge, UK.

Neukum, G., Wagner, R., Denk, T., Porco, C.C., 2005. The cratering record of the saturnian satellites Phoebe, Tethys, Dione and Iapetus in comparison: First results from analysis of the Cassini ISS imaging data. Lunar Planet. Sci. XXXVI. Abstract 2034.

Pike, R.J., 1977. Size-dependence in the shape of fresh impact craters on the Moon. In: Roddy, D.J., Pepin, R.O., Merrill, R.B. (Eds.), Impact and Explosion Cratering. Pergamon, New York, pp. 489–509.

Porco, C.C., and 34 colleagues, 2005. Cassini imaging science: Initial results on Phoebe and Iapetus. Science 307, 1237–1242.

Parmentier, E.M., Head, J.W., 1981. Viscous relaxation of impact craters on icy planetary surfaces: Determination of viscosity variation with depth. Icarus 47, 100–111.

Schenk, P.M., 1989. Crater formation and modification on the icy satellites Uranus and Saturn: Depth/diameter and central peak occurance. J. Geophys. Res. 94 (B4), 3813–3832.

Schenk, P.M., 1991. Ganymede and Callisto: Complex crater formation and planetary crusts. J. Geophys. Res. 96, 15635–15664.

Smith, B.A., and 26 colleagues, 1981. Encounter with Saturn: Voyager 1 imaging science results. Science 212, 163–191.

Smith, B.A., and 28 colleagues, 1982. A new look at the Saturn system: The Voyager 2 images. Science 215, 504–537.

Spencer, J.R., Pearl, J.C., Segura, M., 2005. Iapetus surface temperatures, and the influence of sublimation on the albedo dichotomy: Cassini CIRS constraints. Bull. Am. Astron. Soc. 37. Abstract 39.08.

Stooke, P.J., 2002. Tethys and Dione: New geological interpretations. Lunar Planet. Sci. XXXIII. Abstract 1553.

Thomas, P.C., and 14 colleagues, 2008. Shapes of the saturnian icy satellites and their significance. Icarus 190, 573–584.

Vilas, F., Jarvis, K.S., Barker, E.S., Lederer, S.M., Kelley, M.S., Owen, T.C., 2004. Iapetus dark and bright material: Giving compositional interpretation some latitude. Icarus 170, 125–130.

Wood, C.A., Head, J.W., 1976. Comparison of impact basins on Mercury, Mars, and the Moon. Proc. Lunar. Sci. Conf. 7, 3629–3651.